Volume 10 | Number 20 | 21 October 2023

10 YEARS ANNIVERSARY

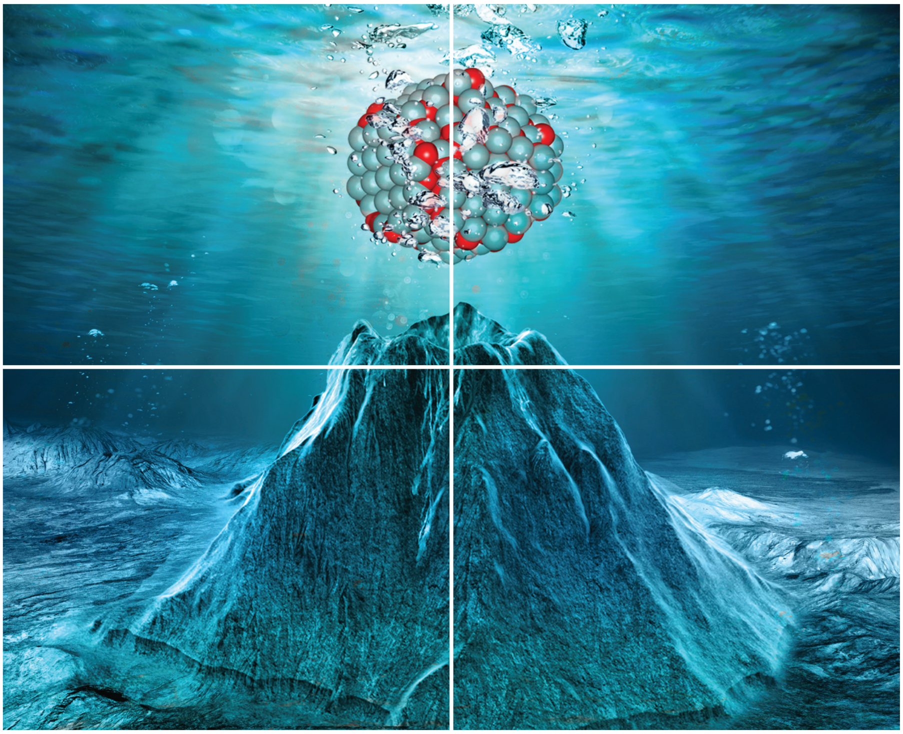

INORGANIC CHEMISTRY FRONTIERS

CCS 中国化学会 CHINESE CHEMICAL SOCIETY

PEKING UNIVERSITY 1898

ROYAL SOCIETY OF CHEMISTRY

rsc.li/frontiers-inorganic

INORGANIC CHEMISTRY FRONTIERS

CHINESE CHEMICAL SOCIETY · ROYAL SOCIETY OF CHEMISTRY

RESEARCH ARTICLE

View Article Online
View Journal | View Issue

Open Access Article. Published on 21 June 2023. Downloaded on 2/2/2026 12:10:38 PM.
This article is licensed under a Creative Commons Attribution-NonCommercial 3.0 Unported Licence.

Check for updates

Cite this: *Inorg. Chem. Front.*, 2023, **10**, 5885

Ru-based nanoparticles supported on carbon nanotubes for electrocatalytic hydrogen evolution: structural and electronic effects†

Nuria Romero, *‡[a,b] Dídac A. Fenoll,‡[a] Laia Gil, [a] Sergi Campos,[a] Jordi Creus, [a,b] Gerard Martí, [a] Javier Heras-Domingo, [a] Vincent Collière,[b] Camilo A. Mesa, [c] Sixto Giménez, [c] Laia Francàs, [a] Luis Rodríguez-Santiago, [a] Xavier Solans-Monfort, *[a] Mariona Sodupe, [a] Roger Bofill, [a] Karine Philippot, *[b] Jordi García-Antón [a] and Xavier Sala *[a]

Received 16th April 2023,
Accepted 20th June 2023

DOI: 10.1039/d3qi00698k

rsc.li/frontiers-inorganic

The performance of Ru-based nanoparticles (NPs) in the hydrogen evolution reaction (HER) relies on both their structural properties and the oxidation state of the metal. Herein, the versatility of the organometallic approach for the synthesis of metal-based nanostructures is combined with thermal oxidation treatments to prepare carbon-nanotube (CNT)-supported Ru-containing nanomaterials for their use as electrocatalysts after dropcasting onto a glassy carbon rotating disk electrode. This strategy allowed access to a series of hybrid nanomaterials of different Ru/RuO_2 compositions and different structural order. Linear sweep voltammetry experiments show that the relative disposition of the Ru/RuO_2 phases, their interconversion under reductive turnover conditions and the degree of structural order affect the HER electrocatalytic performance of different materials. The electrode containing NPs consisting of a RuO_2 core and metallic Ru at the surface outperforms that containing either pure RuO_2 NPs or Ru NPs. Impedance spectroscopy studies and DFT calculations suggest that this catalytic activity enhancement arises from improved charge transport properties and from the structure of the exposed metallic Ru shell, which is partially oxidized and highly amorphous.

1. Introduction

The imperative need for supplanting fossil fuels with clean and renewable energy sources to mitigate climate change enforces the development of new renewable energy technologies.[1–3] The production of hydrogen (H_2) by the water splitting (WS) process that can be triggered either by green electricity or direct sunlight conversion is a promising strategy.[4] In this endeavor, the design of cheap, active, and stable electrocatalysts to accelerate the involved processes, namely, the oxygen evolution reaction (OER) and the hydrogen evolution reaction (HER), is essential for achieving a worthwhile complete catalytic WS process.

Metal-based nanoparticles (NPs), with high surface to volume ratios and good stability, are known to be very efficient and selective (electro)catalytic materials for many transformations,[5] among which HER stands as a highly attractive example.[6,7] In acidic media, Pt remains as the state-of-the-art metal. However, Ru-based nanomaterials have recently emerged as potential alternatives to Pt,[8] with improved stability along the overall pH range and competitive kinetics (appropriate Gibbs free energy of the M–H bond)[9] when properly designed.[10] However, compared to Pt NPs, Ru NPs show larger cohesive energy,[11] making them prone to agglomeration under turnover conditions. Thus, the dispersion and immobilization of NPs onto a conductive support is a key strategy to achieve an electrocatalyst with optimal long-term performance, not only preventing the aggregation of metal sites but also improving the electronic communication between the catalyst and the electrode.[6,7,10]

Among conductive supports, carbon-based nanomaterials are commonly used in electrocatalytic applications due to their robustness, chemical inertness, and availability on a large

---

[a] Departament de Química, Universitat Autònoma de Barcelona, Bellaterra, Cerdanyola del Vallès, 08193 Catalonia, Spain. E-mail: xavier.sala@uab.cat, xavier.solans@uab.cat

[b] CNRS, LCC (Laboratoire de Chimie de Coordination), UPR8241, Université de Toulouse, UPS, INPT, F-31077 Toulouse cedex 4, France. E-mail: nuria.romero@lcc-toulouse.fr, karine.philippot@lcc-toulouse.fr

[c] Institute of Advanced Materials (INAM), Universitat Jaume I, Avenida de Vicent Sos Baynat, s/n, 12006 Castelló de la Plana, Castellón, Spain

† Electronic supplementary information (ESI) available. See DOI: https://doi.org/10.1039/d3qi00698k

‡ These authors contributed equally to this work.

Open Access Article. Published on 21 June 2023. Downloaded on 2/2/2026 12:10:38 PM.
This article is licensed under a Creative Commons Attribution-NonCommercial 3.0 Unported Licence.

scale in a wide range of well-defined shapes and sizes.[12] Of particular interest are carbon-nanotubes (CNTs), which show a highly exposed surface area, metal-like conductivity, good chemical resistance and stability, as well as appropriate hydrophilicity,[13] which are suitable properties for electrocatalytic applications in aqueous media.[14] In this context, CNTs have been shown to be effective at stabilizing Ru NPs on hybrid electrodes for the HER.[15–22] Globally, the effect of (i) functionalizing the CNT surface by oxidative methods,[17,19] (ii) doping the CNT support with one or more elements (*i.e.* N, B, Co/N),[20,22] and (iii) combining Ru with another element to modulate the NP electronic properties (*i.e.* RuP_2 or B-doped Ru), on the overall electrocatalytic performance, has been reported.[18,21] It is worth mentioning that even though the as-synthesized mixtures of Ru and RuO_2 phases have been identified as the best-performing Ru–CNT electrocatalysts,[16,17] their interconversion under reductive turnover conditions and their respective (or synergistic) role in the ultimate HER performance have not been studied in detail. Also, the effect of the structural properties (crystalline/amorphous) of the CNT-supported Ru/RuO_2 electrocatalysts on the HER activity has not yet been discussed. To study the influence of these parameters, we combined the organometallic approach for the synthesis of nanostructures,[23,24] an efficient method to obtain small NPs with a narrow size-distribution and controllable surface properties, with thermal oxidation treatments of CNTs in order to obtain a series of CNT-supported Ru-based NPs of varied Ru/RuO_2 compositions and different structural orders, and test their electrocatalytic activity in the HER. The monitoring of the evolution of these nanomaterials under reductive turnover conditions, combined with the DFT modelling of their structures and computed H-adsorption energies, has allowed us to establish a correlation between the characteristics of the CNT-supported Ru-based NPs and their electrocatalytic properties in the HER.

2. Experimental

2.1. Synthetic procedures

All operations for the synthesis of **Ru/CNT** nanomaterials were carried out using standard Schlenk tubes, Fisher Porter bottle techniques or in a glove box (MBraun) under an argon atmosphere. Solvents (THF and hexane) were purified before use by distillation under a N_2 atmosphere with a drying agent (sodium + benzophenone or CaH_2, respectively) and degassed according to a freeze–pump–thaw process. The ruthenium precursor, [Ru(COD)(COT)] (COD = 1,5-cyclooctadiene; COT = 1,3,5-cyclooctatriene) was purchased from Nanomeps, Toulouse. Ru(IV) oxide 99.9% purity was purchased from Merck. Hydrogen gas with a purity of 5.0 was purchased from Abelló Linde, S.A. CNTs were purchased from Nanostructured & Amorphous Materials, Inc. (Texas, USA) with 99.9% purity and an OD of 50–80 nm and a length of 10–20 μm. High purity deionized water was obtained by passing distilled water through a nanopore Milli-Q water purification system.

2.1.1. Synthesis of Ru@RuO_2/CNT. In a Fisher Porter reactor, 20 mg of CNTs were dispersed in 20 mL of dried and degassed THF in an ultrasound bath for 30 min. Then, 7 mg (0.045 mmol) of [Ru(COD)(COT)] was added to the reactor inside a glove box. After pressurization of the reactor with 3 bar H_2 at room temperature, the initial yellow solution turned dark brown in a few minutes. Vigorous magnetic stirring and H_2 pressure were maintained for 2 h. Then, the H_2 pressure was evacuated. A drop of the colloidal suspension was deposited onto a carbon-covered copper grid for TEM analysis, and the Ru nanomaterial was isolated as a black powder after centrifugation and washing with THF and hexane and drying under vacuum. ICP-OES: (Ru wt%): 5%.

2.1.2. Synthesis of RuO_2-10′/CNT and RuO_2-120′/CNT. The as-synthesized **Ru@RuO_2/CNT** nanomaterial was oxidized at 300 °C under ambient air inside a furnace for 10 min and 120 min, leading to **RuO_2-10′/CNT** and **RuO_2-120′/CNT** nanomaterials, respectively. The furnace was pre-heated at 300 °C before sample introduction.

2.1.3. Electrode preparation. A 2 mg mL^{-1} dispersion was prepared by adding 1 mg of each nanomaterial to 500 μL of THF and sonicating for 30 min. Then, a 5 μL aliquot of this dispersion was added to the surface of a glassy carbon rotating disk electrode (GC-RDE, ∅ = 0.3 cm, S = 0.07 cm^2) or an FTO electrode for the faradaic efficiency measurements, and dried under a N_2 flow.

2.2. Characterization techniques

2.2.1. Transmission electron microscopy (TEM) and high-resolution TEM (HRTEM). TEM images was performed at the "Servei de Microscòpia de la UAB" using a JEOL JEM 2010 electron microscope, and HRTEM at the "Centre de Microcaractérisation Raimond Castaing" in Toulouse (UMS-CNRS 3623) on a JEOL JEM-ARM 200F microscope working at 200 kV with a point resolution of 0.19 nm. Samples for TEM analyses were prepared by slow evaporation of a drop of the crude dispersion deposited onto a holey carbon-covered copper grid. Samples for HRTEM analyses were prepared in the same way from purified nanomaterials redispersed in THF. TEM allowed the evaluation of NP mean size, size distribution, dispersion and morphology. Enlarged micrographs were used for treatment using ImageJ software to obtain a statistical size distribution and the mean diameter of NPs. The analyses were performed assuming that the NPs are spherical. NP sizes are quoted as the mean diameter ± the standard deviation. FFT treatments of HRTEM images were carried out using Digital Micrograph Version 1.80.70 to determine the crystalline structure of the Ru NPs.

2.2.2. X-Ray photoelectron spectra (XPS). Measurements were performed at the Catalan Institute of Nanoscience and Nanotechnology (ICN2) in Barcelona with a Phoibos 150 analyzer (SPECS GmbH, Berlin, Germany) under ultra-high vacuum conditions (base pressure 5^{-10} mbar) with a monochromatic aluminium Kalpha X-ray source (1486.74 eV). The energy resolution was measured by the FWHM of the Ag $3d_{5/2}$ peak for a sputtered silver foil, which was 0.62 eV.

Open Access Article. Published on 21 June 2023. Downloaded on 2/2/2026 12:10:38 PM.
This article is licensed under a Creative Commons Attribution-NonCommercial 3.0 Unported Licence.

2.2.3. Inductively coupled plasma optical emission spectrometry (ICP-OES). Measurements were performed on an Optima 4300DV PerkinElmer system at UAB (Chemical Analysis Service). Samples were prepared by taking 5 mg of the nanomaterials and digesting them with aqua regia under microwave conditions followed by dilution of the mixture with HCl 1% (v/v).

2.2.4. Electrochemical measurements. All the electrochemical experiments were performed using a BioLogic SP-150 potentiostat. A glassy carbon rotating disk electrode (GC-RDE, ∅ = 0.3 cm, S = 0.07 cm^2) was used as the working electrode (WE). A Pt grid was used as the counter electrode (CE) and a saturated calomel electrode (SCE, KCl sat.) was used as a reference electrode (RE). All data were transformed to RHE by applying +0.241 V. The rotating disk electrode (RDE) was set at 3000 rpm in order to ensure the complete removal of *in situ* formed gas bubbles. The solutions were degassed previously for the electrochemical analysis with a N_2 flow. Ohmic potential (IR) drop was automatically corrected at 85% using the Biologic EC-Lab software for cyclic voltammetry and chronoamperometry. For chronopotentiometry experiments the IR drop was manually corrected ($E_{mod} = E_{meas} + E_{IR}$, mod = modified and means = measured) at 85% by adding the corresponding potential value $E_{IR} = i_{exp} \times (R_{mes} \times 0.85)$, where i_{exp} is the applied current in A and R_{mes} is the measured resistance in Ω. A 1 M H_2SO_4 solution was prepared by mixing 56.1 mL of 95–97% H_2SO_4 in 1 L of Milli-Q water.

A Unisense H2-NP Clark type electrode was used to measure the produced hydrogen in the gas phase during the chronopotentiometry experiments by placing it together with the WE (in this case a FTO electrode) and RE (in this case Ag/AgCl) in the same compartment. Faradaic efficiencies were calculated for each system. The sensor was calibrated by adding different known volumes of 99% pure hydrogen at the end of the experiment.

Linear sweep voltammetry (LSV). For LSV, a 20 mL vial was used as an electrochemical cell. For HER experiments, the system was scanned from E_i = 0.400 V to E_f = −0.360 V *vs.* RHE at a scan rate of 10 mV s^{-1} unless otherwise stated.

Chronopotentiometry (CP). Controlled current intensity experiments were performed at j_{app} = −10 mA cm^{-2} for the time indicated in each case.

2.2.5. Electrochemical impedance spectroscopy (EIS). The EIS measurements were performed on a PGSTAT302N potentiostat (Metrohm-Autolab, The Netherlands) using the same conditions described for the electrochemical measurements, *i.e.*, with the catalysts immobilized onto a GC electrode and using a saturated calomel electrode (SCE, KCl sat.) as the reference electrode. EIS measurements were carried out at selected applied potentials with a sinusoidal perturbation of 10 mV and a frequency range from 100 kHz to 0.1 Hz.

2.3. Computational details

2.3.1. Models. DFT calculations were performed to rationalize the differences observed for the NPs present in **r-Ru@RuO₂/CNT/GC** and **r-RuO₂-10′/CNT/GC**. The NPs in **r-RuO₂-10′/CNT/GC** were modelled with three non-polar slab models that differ in the Ru content above and below the RuO_2 slab (*vide infra*): (i) the **RuO₂@Ru₇** model is formed by a seven Ru atom aggregate with a close packed plane structure, (ii) the **RuO₂@Ru₁₀** model is formed by a small NP model containing two close packed planes with 7 and 3 atoms, respectively, and finally (iii) the **RuO₂@Ru₂₀** model implies a full Ru layer with a close packed plane structure over RuO_2. The RuO_2 rutile-like structure in these three models was represented by a (3 × 2) supercell four-layer slab model of the most stable (110) surface to give enough space to fit the **RuO₂@Ru₇** and **RuO₂@Ru₁₀** models and avoid a large mismatch (less than 6%) with the Ru monolayer of the **RuO₂@Ru₂₀** model. The Ru monolayer of **RuO₂@Ru₂₀** corresponds to a $(5 \times 2\sqrt{3}R30°)$ supercell of crystalline Ru.[25] The final cell parameters are a = 9.4609 Å, b = 13.6556 Å and c = 35 Å. The NPs in **r-Ru@RuO₂/CNT/GC** were modelled with the same $(5 \times 2\sqrt{3}R30°)$ supercell of a crystalline 8 layered Ru hexagonal close packed (100) slab model (Ru). Finally, a $(5 \times 2\sqrt{3}R30°)$ supercell of a crystalline 9-layers cubic close packed (111) slab of platinum (Pt) was also considered as a reference system.

2.3.2. Level of theory. All calculations were performed with the PBE[26] density functional as implemented in VASP.[27,28] The dispersion forces were considered by adding Grimme's D2 empirical correction.[29] Atomic cores are described with PAW pseudopotentials[30,31] and the valence electrons are represented with a plane-wave basis set with an energy cutoff of 500 eV. The first Brillouin zone is described with a (4,4,1) Monkhorst–Pack K-point mesh.[32] The energy convergence criteria are fixed to 10^{-5} and 10^{-4} eV for electronic and geometry relaxations, respectively. This methodology is equivalent to that previously used by our research group when modeling RuO_2 and IrO_2 surfaces[33,34] and their electrocatalytic activity.[35,36] Bader charge analysis[37,38] was performed to analyze the influence of the Ru charge on the H adsorption energy.

H adsorption energies reported along the text are mean values that were computed as proposed by Nørskov and coworkers[39] and summarized in eqn (1):

$$E_{\mathrm{ads}} = [E_{n\mathrm{H\text{-}surf}} - (E_{\mathrm{surf}} + nE_{\mathrm{H_2}}/2)]/n, \tag{1}$$

where $E_{nH\text{-}surf}$, E_{surf} and E_{H_2} are the energies of the surface with adsorbed hydrogen atoms, of the clean surface and of the H_2 molecule, respectively; n stands for the number of hydrogen atoms. For coverages higher than 1 hydrogen per unsaturated metal center, the adsorption energies were computed with respect to the 1 hydrogen per Ru center coverage as shown in eqn (2):

$$E_{\mathrm{ads}} = [E_{(N+1)\mathrm{H\text{-}surf}} - (E_{N\mathrm{H\text{-}surf}} + E_{\mathrm{H_2}}/2)], \tag{2}$$

where N is the number of accessible ruthenium centers.

Open Access Article. Published on 21 June 2023. Downloaded on 2/2/2026 12:10:38 PM.
This article is licensed under a Creative Commons Attribution-NonCommercial 3.0 Unported Licence.

3. Results and discussion

3.1. Synthesis of CNT-supported Ru-based nanomaterials

Ru(0) NPs were synthesized on the surface of CNTs following the organometallic method,[24,40] which consists of decomposition under mild conditions (3 bar H_2, R.T. 2 h of vigorous stirring) of [Ru(COD)(COT)] (COD = 1,5-cyclooctadiene; COT = 1,3,5-cyclooctatriene) in the presence of multi-walled CNTs in THF (step 1 in reaction (1), Fig. 1, detailed synthetic conditions can be found in the Experimental section). The obtained nanomaterials were then exposed to ambient air (step 2 in reaction (1), Fig. 1) during the purification process (washing with THF and hexane, centrifugation), which induced surface oxidation, yielding core–shell **Ru@RuO$_2$/CNT** nanomaterials. **Ru@RuO$_2$/CNT** was then subjected to oxidative treatment under air at 300 °C for 10 (**RuO$_2$-10′/CNT**) (reaction (2), Fig. 1) or 120 minutes (**RuO$_2$-120′/CNT**) (reaction (3), Fig. 1) to access fully oxidized RuO_2 NPs of different sizes and morphologies (see below).

3.2. Structural, morphological and compositional characterization of CNT-supported Ru-based nanomaterials

The obtained CNT-supported Ru-based nanomaterials were characterized by TEM, HRTEM-EDX and XPS techniques (Fig. 2 and Fig. S1–S5†) to evaluate the dispersion, shape, size distribution and composition of Ru NPs.

TEM and HRTEM analyses showed that the **Ru@RuO$_2$/CNT** nanomaterial contains well dispersed, well defined and highly crystalline NPs of 2.8 ± 0.8 nm average size at the surface of the carbon support (Fig. 2a and S1†). Careful local EDX analysis of individual NPs in a holey carbon covered copper grid showed the presence of only Ru and small amounts of oxygen in all cases (Fig. S2†). XPS analysis (Fig. 2g) revealed the presence of both Ru(0) and RuO_2 in a mixture of *ca.* 0.76 : 0.24, as shown by the Ru $3d_{5/2}$ peaks centered at 280.4 eV and 281.3 eV for metallic Ru and RuO_2, respectively. The presence of both Ru(0) and RuO_2 in the NPs results from a surface passivation phenomenon that commonly occurs under atmospheric oxygen,[9,40–42] yielding core@shell Ru@RuO$_2$ NPs on the CNTs. The crystallinity of the Ru NPs has been confirmed by HRTEM. Electron diffraction patterns obtained after fast Fourier transform (FFT) treatment (Fig. S1†) indicated two families of interplanar distances for individual NPs, namely 0.21, 0.23 and 0.11 nm, that correspond to the (002), (110) and (004) planes of the hexagonal compact crystalline (hcp) structure of bulk Ru (0), and 0.13, 0.12 and 0.25 nm, that correspond to the (022), (111) and (011) planes of the rutile structure of RuO_2.

HRTEM analysis of the **RuO$_2$-10′/CNT** nanomaterial (oxidation in air, 300 °C, 10 min) showed an increase of the average size of the Ru NPs, up to 5.3 ± 0.9 nm (Fig. 2b and S3†). This NP growth may be explained by the diffusion of the NPs along the CNTs during the temperature treatment (sintering) as well as the incorporation of oxygen atoms into the structure upon oxidation of the NP core. As can be observed for the **RuO$_2$-120′/CNT** nanomaterial (Fig. 2c and S4†), the same oxidation treatment for 120 min provoked the coalescence of the NPs and led to the formation of well crystallized Ru-based nanorods (6.7 ± 1.5 nm in width and 24.8 ± 5.5 nm in length). FFT treatment of the HRTEM image or the electron diffraction patterns of **RuO$_2$-10′/CNT** and **RuO$_2$-120′/CNT** nanomaterials (Fig. S3 and S5,† respectively) indicate interplanar distances of 0.13, 0.16, 0.17 and 0.25 nm, which agree with the (202), (220), (211) and (101) planes of the rutile structure of RuO_2. XPS analyses of the **RuO$_2$-10′/CNT** and **RuO$_2$-120′/CNT** nanomaterials (Fig. 2h and i) confirmed the complete oxidation of the as-prepared Ru@RuO$_2$ NPs, the unique peak is observed at 280.8 eV corresponding to the Ru $3d_{5/2}$ band of RuO_2. This is corroborated by EDX analysis, where the presence of Ru and O elements in high amounts is detected for both samples (Fig. S3 and S4†).

3.3. Electrocatalytic HER studies

The **Ru@RuO$_2$/CNT**, **RuO$_2$-10′/CNT** and **RuO$_2$-120′/CNT** nanomaterials were dispersed in THF and the obtained suspensions were dropcast onto a glassy carbon (GC) rotating disk electrode. The so-obtained **Ru@RuO$_2$/CNT/GC**, **RuO$_2$-10′/CNT/GC**, and **RuO$_2$-120′/CNT/GC** were introduced as working electrodes in a three-electrode cell in 1 M H_2SO_4 and then subjected to a reductive treatment (20 min chronopotentiometry (CP) at -10 mA cm^{-2}),[9,43] leading to the corresponding reduced

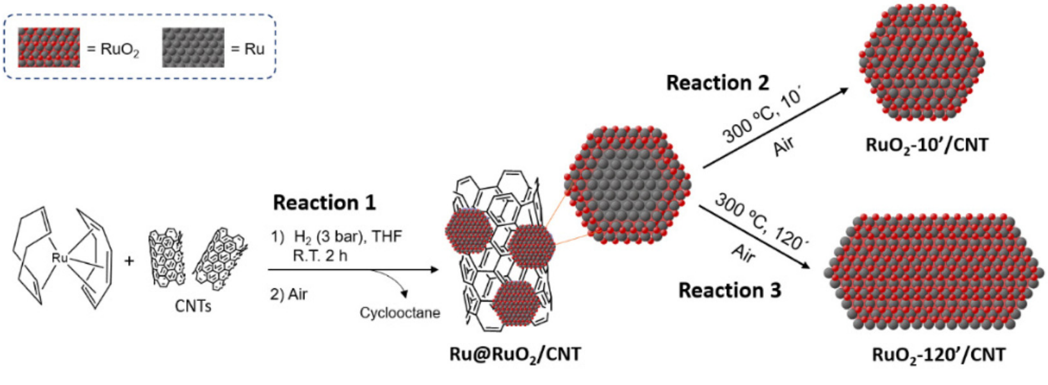

Fig. 1 Scheme of the synthesis of CNT-supported Ru-based nanomaterials.

Open Access Article. Published on 21 June 2023. Downloaded on 2/2/2026 12:10:38 PM.
This article is licensed under a Creative Commons Attribution-NonCommercial 3.0 Unported Licence.

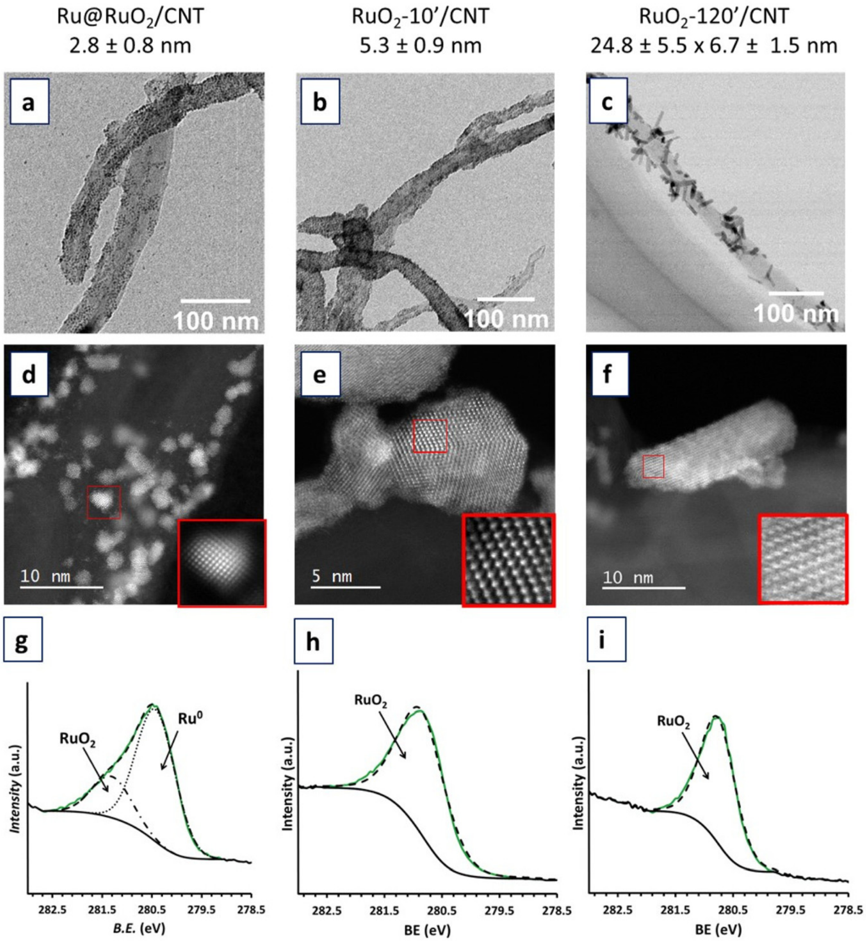

Fig. 2 TEM images, HRTEM images and XPS spectra of **Ru@RuO$_2$/CNT** (a, d and g), **RuO$_2$-10′/CNT** (b, e and h) and **RuO$_2$-120′/CNT** (c, f and i) nanomaterials. In the XPS spectra, the RuO_2 component is shown by a dotted-dashed black line, the Ru(0) component by a dotted black line, the envelope by a dashed black, the experimental data by a solid green line and the background signal by a solid black line.

counterparts: **r-Ru@RuO$_2$/CNT/GC**, **r-RuO$_2$-10′/CNT/GC**, and **r-RuO$_2$-120′/CNT/GC** ("r-" will be used from now on for all hybrid nanomaterials exposed to a reductive potential). Linear sweep voltammetry (LSV) experiments under reductive potentials (from 0.40 V to −0.35 V *vs.* RHE) were recorded for both the as-synthesized and reduced nanomaterials to evaluate their electrocatalytic performance in the HER. The LSV plots and the main benchmarking parameters are presented in Fig. 3 and Table S1,† respectively.

The **Ru@RuO$_2$/CNT/GC** electrode shows an onset overpotential of 200 mV (η_0 = 200 mV) and a current density of 10 mA cm^{-2} is achieved at an overpotential of 272 mV (η_{10} = 272 mV) (Fig. 3a, dashed). However, a clear shift of the polarization curve is observed for its reduced counterpart (**r-Ru@RuO$_2$/CNT/GC**), which shows a decrease in both overpotentials by 50 mV (Fig. 3a, bold) to η_0 = 150 mV and η_{10} = 222 mV. XPS analysis of the **r-Ru@RuO$_2$/CNT** nanomaterial (Fig. S6b†) shows the total disappearance of the RuO_2 phase, leading to a pure Ru(0)-based nanomaterial. Given the already described superior HER activity of the Ru(0) phase over the RuO_2 one, the disappearance of the RuO_2 phase after the reductive treatment by chronopotentiometry can explain the detected enhancement in HER activity.[41,43]

The electrocatalytic enhancement after negative bias is even more evident when comparing the HER electro-activity of the **RuO$_2$-10′/CNT/GC** electrode and that of its reduced counterpart, **r-RuO$_2$-10′/CNT/GC** (Fig. 3b); η_0 and η_{10} decrease from 130 to 50 mV and from 319 to 115 mV, respectively, and the Tafel slope (Fig. S7†) drops from 289 to 77 mV dec^{-1}. XPS analysis of the **r-RuO$_2$-10′/CNT/GC** nanomaterial shows an asymmetric XPS peak that includes both RuO_2 (Ru 3d$_{5/2}$ – 281.3 eV) and metallic Ru (Ru 3d$_{5/2}$ – 280.4 eV) components (Fig. S6c†), with an approximate contribution of 85% and 15%, respectively. The observed activation in the HER may thus arise from the formation of highly active Ru metal atoms, that may eventually form a thin shell on the top of the initial RuO_2 core (see Fig. S6a,† bottom). Interestingly, the HER activity of the **r-RuO$_2$-10′/CNT/GC** electrode, with a RuO_2 core and metallic Ru at the surface, outperforms that of the **r-Ru@RuO$_2$/CNT/GC** electrode, where only metallic Ru is present. Also, the faradaic

Open Access Article. Published on 21 June 2023. Downloaded on 2/2/2026 12:10:38 PM.
This article is licensed under a Creative Commons Attribution-NonCommercial 3.0 Unported Licence.

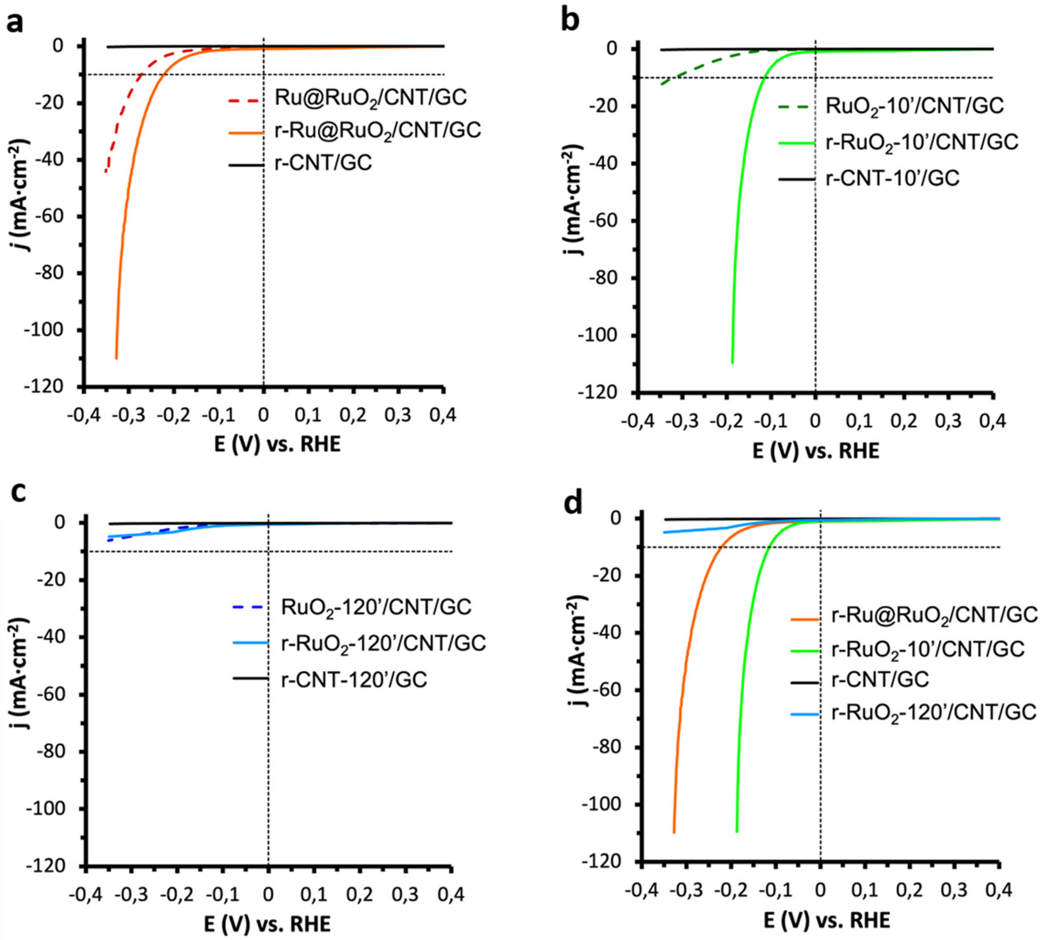

Fig. 3 LSVs in 1 M H_2SO_4 of (a) **Ru@RuO$_2$/CNT/GC** (dashed red line) and **r-Ru@RuO$_2$/CNT/GC** (orange line), (b) **RuO$_2$-10′/CNT/GC** (dashed green line) and **r-RuO$_2$-10′/CNT/GC** (light green line) and (c) **RuO$_2$-120′/CNT/GC** (dashed blue line) and **r-RuO$_2$-120′/CNT/GC** (light blue line), before and after a 20 min reductive chronopotentiometry at j = −10 mA cm^{-2}, respectively; (d) comparison of polarization curves of **r-Ru@RuO$_2$/CNT/GC** (orange), **r-RuO$_2$-10′/CNT/GC** (light green line) and **r-RuO$_2$-120′/CNT/GC** (light blue line) after a 20 min reductive chronopotentiometry at j = −10 mA cm^{-2}. The LSV curve corresponding to each **r-CNT-*X*/GC** (X = 0-, 10- or 120-minutes oxidation at 300 °C) blank (no catalyst present) is shown in black. The thermodynamic HER potential in 1 M H_2SO_4 and the reference j = −10 mA cm^{-2} current density are indicated as black dashed lines.

efficiency of both reduced nanomaterials was evaluated on larger surface-area fluorine doped tin oxide (FTO) electrodes (Fig. S8†). The attained >98% value confirms the production of H_2 as the sole reaction happening under turnover conditions.

In contrast, the nanomaterials resulting from a 120 min thermal treatment in both as-synthesized and cathodically polarized versions (**RuO$_2$-120′/CNT/GC** and **r-RuO$_2$-120′/CNT/GC**) showed negligible HER electro-activity (Fig. 3c). These results indicate that the presence of large and highly crystalline RuO_2 nanorods on the electrode is not favorable for the HER activity, clearly highlighting the influence of the duration of the applied thermal treatment on the electrocatalytic performance. Similar results (poor electro-activity of both as-received and cathodically polarized counterparts) were obtained when the HER performance of bulk commercial RuO_2 was assayed under identical electrocatalytic conditions (Fig. S9†). This is also in accordance with previous reports where a decrease in the HER activity of hydrous RuO_2 NPs was observed after enhancing their crystallinity through annealing processes.[44,45] Given the inactivity of the **RuO$_2$-120′/CNT/GC** and **r-RuO$_2$-120′/CNT/GC** samples in the HER, these electrodes have not been studied further.

With the aim at better understanding the reasons behind the activity trends in the HER described in this section, impedance spectroscopy (EIS) measurements (Section 3.4) and DFT calculations (Section 3.5) have been performed (*vide infra*).

3.4. Impedance spectroscopy studies

Impedance spectroscopy experiments were first carried out on the as-received CNT supports and their 10′ annealed (air, 300 °C) counterparts. A Randles equivalent circuit was used to fit the experimental data (see Fig. S10† and its inset for a typical Nyquist plot and the equivalent circuit, respectively). Accordingly, capacitance (C) and charge transfer resistance

Open Access Article. Published on 21 June 2023. Downloaded on 2/2/2026 12:10:38 PM. This article is licensed under a Creative Commons Attribution-NonCommercial 3.0 Unported Licence.

(R_{CT}), as well as series resistance (R_S) were obtained. No difference was observed between the as-received and 10′-annealed CNTs (Fig. S11†).

Analogous analyses were performed on the **r-Ru@RuO$_2$/CNT/GC**, **RuO$_2$-10′/CNT/GC** and **r-RuO$_2$-10′/CNT/GC** electrodes in order to define the reasons behind their different HER behaviors (Fig. 4).

When comparing the best performing **r-RuO$_2$-10′/CNT/GC** electrode with its oxidized counterpart, **RuO$_2$-10′/CNT/GC**, the former presents a lower capacitance and charge transfer resistance before the catalytic region (Fig. 4a and b). This observation is consistent with a decrease in the contribution of the RuO$_2$ phase due to the reductive treatment. Interestingly, the measured uncompensated resistance (series resistance, R_S) of this **r-RuO$_2$-10′/CNT/GC** electrode is four times lower than those for **r-Ru@RuO$_2$/CNT/GC** and **RuO$_2$-10′/CNT/GC**, suggesting improved charge transport within the conductive support and further charge extraction due to the thermal oxidation followed by electrochemical reduction (Fig. 4c). However, the three systems present a series resistance (R_S) lower than the charge transfer resistance (R_{CT}) in the catalytic region. This observation indicates that the whole process is limited by the catalyst kinetics rather than the cell resistance.

3.5. DFT calculations

To get further insight into the origin of the high catalytic activity of the NPs in **r-RuO$_2$-10′/CNT/GC**, we performed DFT (PBE-D2)[26,29] periodic calculations (see the Computational details in Section 2.3 for more information). The NPs in **r-RuO$_2$-10′/CNT/GC** were represented with three different slab models, covering different amounts of Ru over a crystalline RuO$_2$ surface (Fig. 5). A Ru surface, as a model of NPs in **r-Ru@RuO$_2$/CNT/GC**, and a Pt surface, as a reference material, were also considered for comparison. The nomenclature of the computational models is Ru and Pt for the metallic systems, and **RuO$_2$@Ru$_N$** for the models of NPs in **r-RuO$_2$-10′/CNT/GC** (N indicates the number of Ru atoms over the RuO$_2$ surface).

According to Nørskov and co-workers, the H adsorption energy can be used as a descriptor of the electrocatalytic activity in the HER of a specific material.[39,46,47] Therefore, we computed the adsorption energy of H for the five models at three different hydrogen coverages (θ), namely 1 hydrogen on the surface ($\theta = 1/N$), 1 hydrogen per Ru surface atom ($\theta = 1$), and one additional hydrogen atom exceeding the 1 hydrogen per Ru center ratio ($\theta = (N + 1)/N$). Several different sites were considered in each case (Fig. 5).

For Ru and Pt surfaces with well-ordered close packed planes, we analyzed three different sites: (1) above a tetrahedral (Td) hole (3_{Td}); (2) above an octahedral (Oh) hole (3_{Oh}) and (3) over a metal atom of the surface (1_{Top}). Alternatively, for **RuO$_2$@Ru$_7$**, **RuO$_2$@Ru$_{10}$** and **RuO$_2$@Ru$_{20}$** we explored several sites covering the most representative environments, including the interaction of H with 3, 2 and 1 Ru centers (Fig. 5). Table 1 reports the highest adsorption energies of the first H atom ($\theta = 1/N$), the mean value of the adsorption energy of one H per Ru surface site ($\theta = 1$) and the adsorption energy range of additional hydrogen atoms after the adsorption of one hydrogen atom per Ru site ($\theta = (N + 1)/N$). Note that in this latter case there are also several potential adsorption sites, from which we considered a selected representative set (Fig. 5b). The adsorption energies of each site with the optimized structures of all considered species can be found in the ESI (Fig. S12–S16†).

At low coverages ($\theta = 1/N$), H adsorbs strongly on Ru (E_{ads}(H) = −71.1 kJ mol^{-1}), with a marked preference for 3_{Oh} sites. The adsorption of H on Pt is weaker (E_{ads}(H) = −58.0 kJ mol^{-1}) and shows no preference for any of the three sites studied. At higher coverages ($\theta = 1$), the same trends are observed, the adsorption of hydrogen on Ru is strong and the adsorption on Pt is weaker (−66.8 *vs.* −50.3 kJ mol^{-1}) and

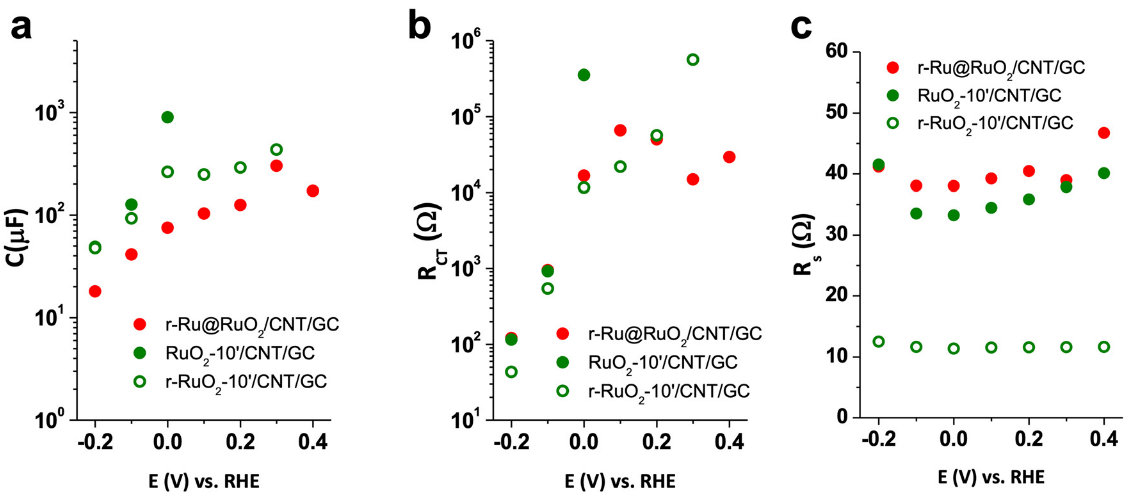

Fig. 4 Impedance spectroscopy results C, R_{CT} and R_S, fitting the Nyquist plots to a simple Randles circuit (see Fig. S9,† inset) for **r-Ru@RuO$_2$/CNT/GC** (red circles), **RuO$_2$-10′/CNT/GC** (green circles) and **r-RuO$_2$-10′/CNT/GC** (green empty circles). (a) Capacitance (C), (b) charge transfer resistance (R_{CT}) and (c) series resistance (R_S).

Open Access Article. Published on 21 June 2023. Downloaded on 2/2/2026 12:10:38 PM.
This article is licensed under a Creative Commons Attribution-NonCommercial 3.0 Unported Licence.

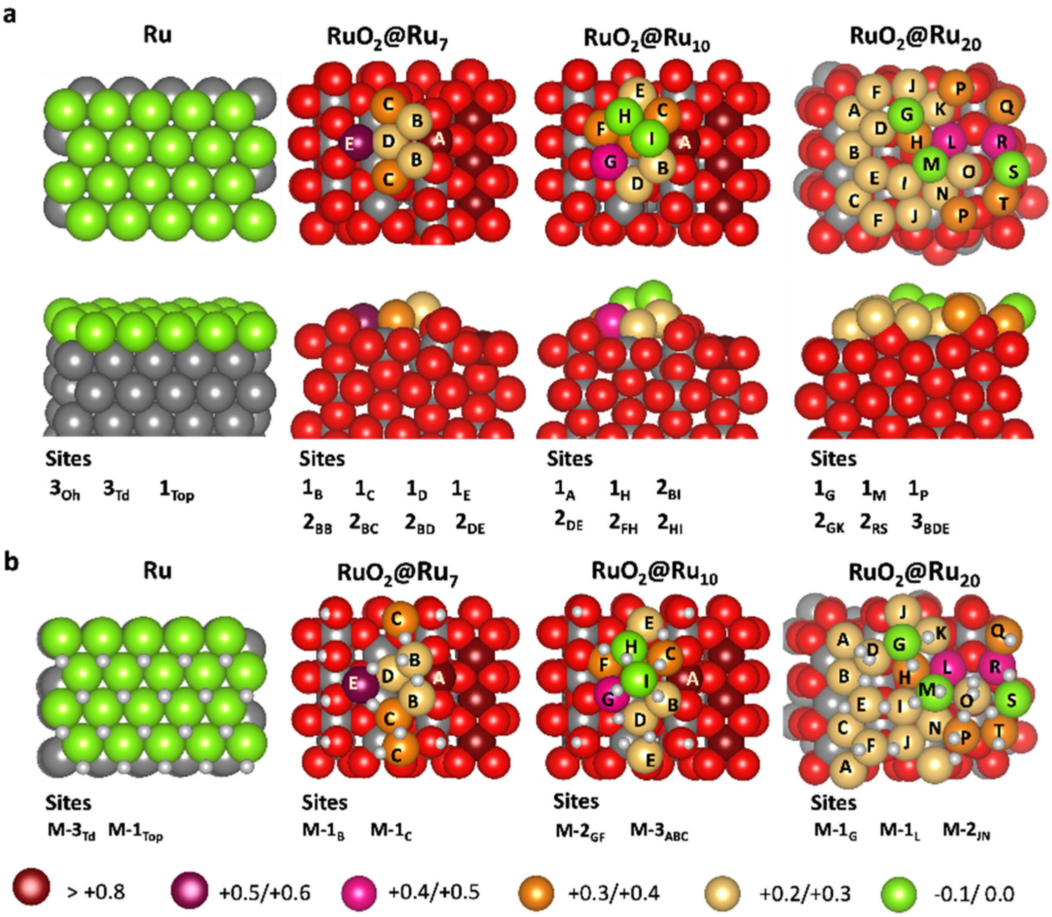

Fig. 5 Studied adsorption sites for (a) the adsorption of one single H atom ($\theta = 1/N$) and (b) the adsorption of one additional H atom to an H monolayer ($\theta = (N + 1)/N$). Site name indicates the number of Ru atoms (1, 2 or 3) interacting with H and the involved centers. Outermost atom color labeling indicates the atomic Bader charges without adsorbed hydrogen. The adsorption energy for each site is reported in the ESI.†

Table 1 Computed (PBE-D2) H adsorption energies (in kJ mol^{-1}) as a function of the material model and hydrogen coverage (θ)

Model	$\theta = 1/N$	$\theta = 1^a$	$\theta = (N+1)/N^b$
Pt	−58.0[a]	−50.3	−32.0 to −34.9
Ru	−71.1[a]	−66.8	+14.1 to +33.8
RuO_2@Ru_7	−76.6 to −49.7[b]	−66.3	−23.5 to −31.2
RuO_2@Ru_{10}	−76.1 to −31.4[b]	−59.7	−27.5 to −32.2
RuO_2@Ru_{20}	−70.7 to −30.5[b]	−57.9	−31.9 to −51.3
	−70.3 to −38.5[c]	−56.6[c]	−20.5 to −55.3[c]

[a] Highest adsorption energy at this H coverage. [b] Range of adsorption energies for this coverage. [c] H adsorption energies computed with a **RuO_2@Ru_{20}** model containing a 8 RuO_2 layer thick core (Fig. S17†).

without a clear preferred site. In both cases, however, the adsorption energies are markedly higher (in absolute value) than those defining a good catalyst according to the Norskøv descriptor ($E_{ads}(H)$ = −23 kJ mol^{-1}).[39] Remarkably, the adsorption of additional H atoms to the monolayer is unfavorable on Ru, but it is still favorable on Pt, with adsorption energies of about −32.0 kJ mol^{-1}. These data suggest that H adsorbs too strongly on Ru at low coverages, thus preventing H_2 evolution. Moreover, at high H coverages (exceeding 1 H per surface Ru center), H_2 evolution on crystalline Ru is hampered by the unfavorable H adsorption. In contrast, while at low coverages H_2 evolution on Pt is also unfavorable due to a strong H adsorption, H adsorption at high coverages is weak and close to the ideal value,[39] and thus H_2 evolution is strongly favored on Pt.

The outermost Ru centers of **RuO_2@Ru_7**, **RuO_2@Ru_{10}** and **RuO_2@Ru_{20}**, which are models of **r-RuO_2-10′/CNT/GC**, show a high degree of amorphization (Fig. 5). This is attributed to the roughness of the (110) RuO_2 surface, which prevents the formation of Ru close packed planes. Consequently, exposed atoms present a lower coordination and the surface does not show well-defined Oh, Td and Top sites. The adsorption energy of H on **RuO_2@Ru_7**, **RuO_2@Ru_{10}** and **RuO_2@Ru_{20}** at low coverage ($\theta = 1/N$) ranges from −76.6 to −30.5 kJ mol^{-1}, depending on the number of Ru centers interacting with the adsorbed hydrogen and their charges (*vide infra*). In all cases, the adsorption energy of the sites presenting the strongest interaction with H of each model is similar to the values computed for Ru, but there are also several sites where H adsorbs

This journal is © the Partner Organisations 2023

Open Access Article. Published on 21 June 2023. Downloaded on 2/2/2026 12:10:38 PM. This article is licensed under a Creative Commons Attribution-NonCommercial 3.0 Unported Licence.

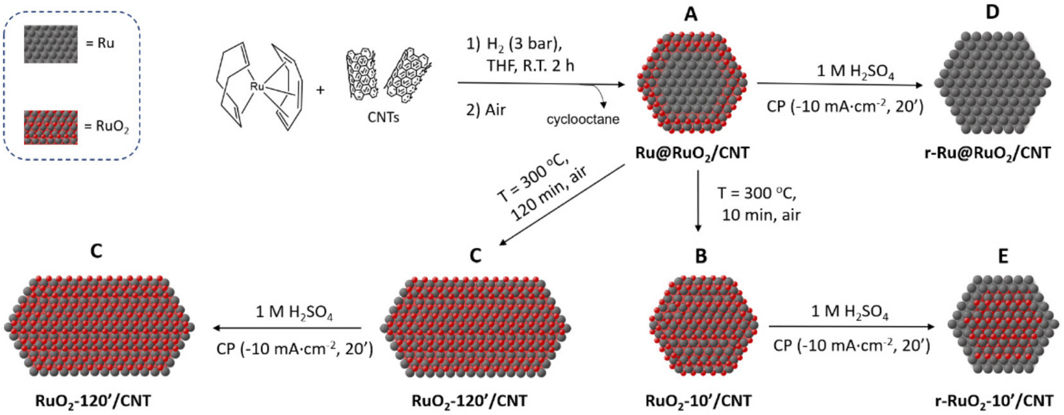

Scheme 1 Proposed scenario for the oxidation/reduction processes occurring at the surface of CNT-supported Ru-based NPs studied in this work. CP = Chronopotentiometry. In **A**–**E** the CNT support has been omitted for the sake of clarity.

more weakly. Indeed, the H adsorption energy tends to increase (in absolute value) upon increasing the number of metal centers that the adsorbed H is interacting with, and on decreasing the positive charge of the Ru centers interacting with H. As a consequence, the final adsorption energies are probably the compromise of three factors: (1) the lower metal coordination in amorphous **RuO_2@Ru_7**, **RuO_2@Ru_{10}** and **RuO_2@Ru_{20}** models that leads to stronger H adsorption; (2) the layer amorphization that hampers the adsorption of H on the ideal Oh sites and (3) the partial oxidation of the external Ru atoms by RuO_2, the latter two factors make the Ru–H interaction weaker.

The average adsorption energies of one H atom per exposed Ru center ($\theta = 1$) are quite similar for the three **RuO_2@Ru_7**, **RuO_2@Ru_{10}** and **RuO_2@Ru_{20}** models (−66.3, −59.7 and −57.9 kJ mol^{-1}, respectively) and close to the value on crystalline Ru (−66.8 kJ mol^{-1}), thus suggesting that H_2 evolution does not arise from coverages below $\theta = 1$. Indeed, the HER takes place when additional H atoms are added to a coverage of $\theta = 1$. In this scenario and in contrast to what is computed for crystalline Ru, the adsorption of one additional H atom on the three models of **r-RuO_2-10′/CNT/GC** is favorable and usually weak, with values ranging between −23.5 and −51.3 kJ mol^{-1}. Indeed, while there are still some sites showing strong adsorption energies, most of the considered centers present values that are similar to those obtained for Pt or even closer to the ideal value. Remarkably, enlarging the RuO_2 core for the **RuO_2@Ru_{20}** model (see Fig. S17†) does not modify the H adsorption energies (Table 1), thus suggesting that the thickness of the RuO_2 core has very little influence on the material catalytic activity. Overall, calculations are in agreement with the higher HER catalytic activity of **r-RuO_2-10′/CNT/GC** when compared to **r-Ru@RuO_2/CNT/GC**, and the calculations suggest that this originates from two factors: (1) the amorphization of the external Ru atoms, that increases the number of hydrogen atoms that can be adsorbed and (2) the partial oxidation of the surface Ru centers by RuO_2, that globally weakens the H adsorption (less negative values).

4. Concluding remarks

In the literature, the performances of the state-of-the-art CNT-supported Ru NP-based HER electrocatalysts are usually discussed on the basis of the as-synthesized Ru/RuO_2 mixtures.[16,17] The interconversion of the two Ru phases that can occur under HER conditions and their respective (or synergistic) role in the ultimate HER performance have not been previously deeply studied, nor the effect of the structural properties (crystalline/amorphous) of these composite materials. In order to clarify these issues, in our study we have combined the organometallic approach for the synthesis of Ru NPs with thermal and electrochemical processes. This allowed us to have at disposal a series of CNT-supported Ru-containing NPs of assorted composition, disposition of the Ru phases and crystalline order, for a comparison of their catalytic activities in the HER (Scheme 1). Our results show that the relative disposition of the Ru/RuO_2 phases, their interconversion under reductive turnover conditions and the degree of structural order in the studied materials affect the HER electrocatalytic performance.

The decomposition of [Ru(COD)(COT)] under H_2 (3 bar, R.T.) in the presence of CNTs followed by air exposure led to a CNT-supported Ru-based nanomaterial with small Ru@RuO_2 core–shell NPs well-dispersed onto the CNTs (Scheme 1, **A**). Subsequent oxidative thermal treatment (ambient air, 300 °C) of this nanomaterial provided CNT-supported RuO_2 NPs (Scheme 1, **B**) and CNT-supported RuO_2 nanorods (Scheme 1, **C**), after a 10 or 120 min treatment, respectively. Reductive chronopotentiometry under HER electrocatalytic conditions (−10 mA cm^{-2}) in acidic medium (1 M H_2SO_4) allowed the reduction of the RuO_2 shell of the Ru@RuO_2 NPs in the as-synthesized nanomaterial **A**, yielding CNT-supported fully metallic Ru NPs (Scheme 1, **D**). An identical CP reductive treatment on the fully oxidized RuO_2 NPs in nanomaterial **B** led to RuO_2@Ru core–shell NPs (Scheme 1, **E**), while the RuO_2 nanorods in **C** remained the same (Scheme 1, **C**). Surface reduction in **C** is prevented by the high reorganizational energy of the

Open Access Article. Published on 21 June 2023. Downloaded on 2/2/2026 12:10:38 PM.
This article is licensed under a Creative Commons Attribution-NonCommercial 3.0 Unported Licence.

highly crystalline RuO_2 surface, giving an inactive nanomaterial in the HER. Interestingly, when applied to the Ru@RuO_2 NPs in **A** or the RuO_2 NPs in **B**, the CP reductive treatment (Scheme 1, **A** → **D** and **B** → **E**) yielded the superior HER electrocatalysts **D** and **E**, respectively. These results highlighted the predominant role of the metallic Ru sites at the NP surface over the RuO_2 ones in the HER.

Even more remarkably, the nanomaterial **E** that contains RuO_2@Ru core–shell NPs showed a superior HER activity than its counterpart **D**, containing fully metallic Ru NPs. In order to rationalize this difference in HER electroactivity, a DFT analysis of the H-adsorption energy values was performed. Periodic slab models were used to mimic the hybrid Ru–RuO_2 nanomaterials in comparison with pure Ru and Pt metal surfaces, with different H coverages. The calculated data of H adsorption energies reproduce the experimental catalytic activity trends and reinforce their use as descriptors for analyzing their HER activity. When the Ru shell is only one layer thick or below, surface amorphization prevents the adsorption of H at the octahedral sites, which weakens the Ru–H interaction and generates additional sites with adsorption energies close to those of Pt. Moreover, the presence of a RuO_2 core weakens the H adsorption energies, bringing them closer to the ideal value. Additionally, the presence of a Ru layer on top of the RuO_2 core yields improved charge transport properties, as demonstrated by EIS measurements. Overall, the **r-RuO_2-10′/CNT/GC** nanomaterial **E**, which contains RuO_2@Ru NPs, shows higher electrocatalytic activity when compared to **D** (pure Ru metal) likely due to two factors: its surface partial oxidation and, more importantly, its amorphization. This amorphization may also explain the high HER electro-activity reported for very small Ru NPs, which are quite amorphous and have numerous surface sites and defects.[9,10] This hypothesis is supported by H adsorption calculations on Ru NPs that highlighted the presence of these less coordinated H atoms.[9,48,49]

All in all, the results obtained using controlled CNT-supported Ru-based nanomaterials have put forward the correlation between the oxidation state of Ru (and its evolution under reductive turnover conditions), the degree of structural order at the NP surface and the H adsorption energies as the key activity descriptors. This work provides valuable guidelines to rationally design Ru-based electrocatalysts of higher performance for the HER.

Author contributions

Conceptualization, N. R., X. S.-M., K. P., and X. S.; investigation, N. R., D. F., L. G., S. C., G. M., J. C., V. C., J. H.-D., L. F., C. M., and V. C.; writing – original draft preparation, R. B., L. F., N. R., X. S.-M., X. S. and J. G.-A.; writing – review and editing, S. G., M. S., L. R.-S., J. C., R. B., K. P., N. R., L. F., J. G.-A., C. M. and X. S.; supervision, X. S.-M., L. R.-S., M. S., J. G.-A., R. B., X. S., N. R., and S. G.; and funding acquisition, X. S.-M., K. P., S. G., L. F., J. G.-A., and X. S. All authors have read and agreed to the published version of the manuscript.

Conflicts of interest

There are no conflicts to declare.

Acknowledgements

This work was financially supported by the MICINN/FEDER projects PID2019-104171RB-I00, PID2020-112715GB-I00, PID2021-128197NA-I00 and TED2021-129237B-I00, the Red Española de Supercomputación (RES) through QHS-2021-3-0016 project, the CNRS, the Univ. Toulouse III – Paul Sabatier and the GDRI HC3A Franco-Catalan action. J. C. thanks the UAB for a PhD grant. G. M. and D. A. F. thank MICINN for their FPU PhD grants. X. S. thanks ICREA for the ICREA Academia prize 2020. L. F. is indebted to the Ramón y Cajal Program (RYC2018-025394-I fellowship). S. G. acknowledges Universitat Jaume I for financial support through the project UJI-B2019-20. C. A. M. acknowledges the Generalitat Valenciana for the APOSTD/2021/251 fellowship. The authors also acknowledge Guillaume Sauthier for XPS analyses.

References

1 X. Li, H. Zhang, Q. Hu, W. Zhou, J. Shao, X. Jiang, C. Feng, H. Yang and C. He, Amorphous NiFe Oxide-based Nanoreactors for Efficient Electrocatalytic Water Oxidation, *Angew. Chem., Int. Ed.*, 2023, **62**, e202300478.

2 Q. Hu, Z. Wang, X. Huang, Y. Qin, H. Yang, X. Ren, Q. Zhang, J. Liu and C. He, A unique space confined strategy to construct defective metal oxides within porous nanofibers for electrocatalysis, *Energy Environ. Sci.*, 2020, **13**, 5097–5103.

3 Q. Hu, Z. Han, X. Wang, G. Li, Z. Wang, X. Huang, H. Yang, X. Ren, Q. Zhang, J. Liu and C. He, Facile Synthesis of Sub-Nanometric Copper Clusters by Double Confinement Enables Selective Reduction of Carbon Dioxide to Methane, *Angew. Chem., Int. Ed.*, 2020, **59**, 19054–19059.

4 N. S. Lewis, Research opportunities to advance solar energy utilization, *Science*, 2016, **351**, aad1920.

5 D. Astruc, F. Lu and J. R. Aranzaes, *Angew. Chem., Int. Ed.*, 2005, **44**, 7852–7872.

6 J. Zhu, L. Hu, P. Zhao, L. Y. S. Lee and K. Y. Wong, *Chem. Rev.*, 2020, **120**, 851–918.

7 S. Fukuzumi and Y. Yamada, Catalytic activity of metal-based nanoparticles for photocatalytic water oxidation and reduction, *J. Mater. Chem.*, 2012, **22**, 24284–24296.

8 Q. Hu, K. Gao, X. Wang, H. Zheng, J. Cao, L. Mi, Q. Huo, H. Yang, J. Liu and C. He, Subnanometric Ru clusters with upshifted D band center improve performance for alkaline hydrogen evolution reaction, *Nat. Commun.*, 2022, **13**, 3958.

9 J. Creus, S. Drouet, S. Suriñach, P. Lecante, V. Collière, R. Poteau, K. Philippot, J. García-Antón and X. Sala, Ligand-Capped Ru Nanoparticles as Efficient

This journal is © the Partner Organisations 2023

Open Access Article. Published on 21 June 2023. Downloaded on 2/2/2026 12:10:38 PM. This article is licensed under a Creative Commons Attribution-NonCommercial 3.0 Unported Licence.

Electrocatalyst for the Hydrogen Evolution Reaction, *ACS Catal.*, 2018, **8**, 11094–11102.

10 J. Creus, J. de Tovar, N. Romero, J. García-Antón, K. Philippot, R. Bofill and X. Sala, Ruthenium Nanoparticles for Catalytic Water Splitting, *ChemSusChem*, 2019, **12**, 2493–2514.

11 Q. Wang, M. Ming, S. Niu, Y. Zhang, G. Fan and J. S. Hu, Scalable Solid-State Synthesis of Highly Dispersed Uncapped Metal (Rh, Ru, Ir) Nanoparticles for Efficient Hydrogen Evolution, *Adv. Energy Mater.*, 2018, **8**, 1801698.

12 N. Karousis, N. Tagmatarchis and D. Tasis, Current progress on the chemical modification of carbon nanotubes, *Chem. Rev.*, 2010, **110**, 5366–5397.

13 J. Sheng and Y. Li, *ACS Appl. Mater. Interfaces*, 2022, **14**, 20455–20462.

14 X. Zhang, Y. Ye, H. Wang and S. Yao, Deposition of platinum-ruthenium nano-particles on multi-walled carbon nano-tubes studied by gamma-irradiation, *Radiat. Phys. Chem.*, 2010, **79**, 1058–1062.

15 B. Santosh, Z. Wu, R. Sai Siddhartha, G. Krishna Prasad, S. S. Ramamurthy, S. Mitra and R. B. Dandamudi, Ruthenium decorated carbon nanoink as highly active electrocatalyst in hydrogen evolution reaction, *Int. J. Hydrogen Energy*, 2016, **41**, 23007–23014.

16 M. Zhang, J. Chen, H. Li, P. Cai, Y. Li and Z. Wen, Ru-RuO_2/CNT hybrids as high-activity pH-universal electrocatalysts for water splitting within 0.73 V in an asymmetric-electrolyte electrolyzer, *Nano Energy*, 2019, **61**, 576–583.

17 D. H. Kweon, M. S. Okyay, S. J. Kim, J. P. Jeon, H. J. Noh, N. Park, J. Mahmood and J. B. Baek, Ruthenium anchored on carbon nanotube electrocatalyst for hydrogen production with enhanced Faradaic efficiency, *Nat. Commun.*, 2020, **11**, 1278.

18 M. Cheng, H. Geng, Y. Yang, Y. Zhang and C. C. Li, Optimization of the Hydrogen-Adsorption Free Energy of Ru-Based Catalysts towards High-Efficiency Hydrogen Evolution Reaction at all pH, *Chem. – Eur. J.*, 2019, **25**, 8579–8584.

19 R. Ding, L. Lin, C. Pei, X. Yu, Q. Sun and H. S. Park, Hierarchical Architectures Based on Ru Nanoparticles/Oxygen-Rich-Carbon Nanotubes for Efficient Hydrogen Evolution, *Chem. – Eur. J.*, 2021, **27**, 11150–11157.

20 M. Fan, X. Chen, M. Zhang, L. Cui, X. He and X. Zou, Highly dispersed Ru nanoclusters anchored on B,N co-doped carbon nanotubes for water splitting, *Inorg. Chem. Front.*, 2022, **9**, 968–976.

21 X. Sun, W. Li, J. Chen, X. Yang, B. Wu, Z. Wang, B. Li and H. Zhang, Boron-induced activation of Ru nanoparticles anchored on carbon nanotubes for the enhanced pH-independent hydrogen evolution reaction, *J. Colloid Interface Sci.*, 2022, **616**, 338–346.

22 Z. Liu, X. Yang, G. Hu and L. Feng, Ru Nanoclusters Coupled on Co/N-Doped Carbon Nanotubes Efficiently Catalyzed the Hydrogen Evolution Reaction, *ACS Sustainable Chem. Eng.*, 2020, **8**, 9136–9144.

23 C. Amiens, B. Chaudret, D. Ciuculescu-Pradines, V. Collière, K. Fajerwerg, P. Fau, M. Kahn, A. Maisonnat, K. Soulantica and K. Philippot, Organometallic approach for the synthesis of nanostructures, *New J. Chem.*, 2013, **37**, 3374–3401.

24 K. Philippot, P. Lignier and B. Chaudret, Organometallic ruthenium nanoparticles and catalysis, *Top. Organomet. Chem.*, 2014, **48**, 319–370.

25 G. Attard and C. Barnes, *Surfaces*, Oxford University Press, 1998.

26 J. P. Perdew, K. Burke and M. Ernzerhof, Generalized Gradient Approximation Made Simple, *Phys. Rev. Lett.*, 1996, **77**, 3865–3868.

27 G. Kresse and J. Hafner, Ab initio molecular dynamics for liquid metals, *Phys. Rev. B: Condens. Matter Mater. Phys.*, 1993, **47**, 558–561.

28 G. Kresse and J. Furthmü, Efficient iterative schemes for ab initio total-energy calculations using a plane-wave basis set, *Phys. Rev. B: Condens. Matter Mater. Phys.*, 1996, **54**, 11169–11184.

29 S. Grimme, Accurate description of van der Waals complexes by density functional theory including empirical corrections, *J. Comput. Chem.*, 2004, **25**, 1463–1473.

30 P. E. Blöchl, C. J. Först and J. Schimpl, The Projector Augmented Wave Method: ab-initio molecular dynamics with full wave functions, *Phys. Rev. B: Condens. Matter Mater. Phys.*, 1994, **50**, 17953–17979.

31 G. Kresse and D. Joubert, From ultrasoft pseudopotentials to the projector augmented-wave method, *Phys. Rev. B: Condens. Matter Mater. Phys.*, 1999, **59**, 1758–1775.

32 H. J. Monkhorst and J. D. Pack, Special points for Brillonin-zone integrations, *Phys. Rev. B: Solid State*, 1976, **13**, 5188–5192.

33 J. Heras-Domingo, M. Sodupe and X. Solans-Monfort, Interaction between Ruthenium Oxide Surfaces and Water Molecules. Effect of Surface Morphology and Water Coverage, *J. Phys. Chem. C*, 2019, **123**, 7786–7798.

34 D. González, B. Camino, J. Heras-Domingo, A. Rimola, L. Rodríguez-Santiago, X. Solans-Monfort and M. Sodupe, BCN-M: A Free Computational Tool for Generating Wulff-like Nanoparticle Models with Controlled Stoichiometry, *J. Phys. Chem. C*, 2020, **124**, 1227–1237.

35 D. González, J. Heras-Domingo, M. Sodupe, L. Rodríguez-Santiago and X. Solans-Monfort, Importance of the oxyl character on the IrO_2 surface dependent catalytic activity for the oxygen evolution reaction, *J. Catal.*, 2021, **396**, 192–201.

36 D. González, M. Sodupe, L. Rodríguez-Santiago and X. Solans-Monfort, Metal coordination determines the catalytic activity of IrO_2 nanoparticles for the oxygen evolution reaction, *J. Catal.*, 2022, **412**, 78–86.

37 R. F. W. Bader, A Quantum Theory of Molecular Structure and Its Applications, *Chem. Rev.*, 1991, **91**, 893–928.

38 G. Henkelman, A. Arnaldsson and H. Jónsson, A fast and robust algorithm for Bader decomposition of charge density, *Comput. Mater. Sci.*, 2006, **36**, 354–360.

Open Access Article. Published on 21 June 2023. Downloaded on 2/2/2026 12:10:38 PM.
This article is licensed under a Creative Commons Attribution-NonCommercial 3.0 Unported Licence.

39 J. K. Nørskov, T. Bligaard, A. Logadottir, J. R. Kitchin, J. G. Chen, S. Pandelov and U. Stimming, Trends in the Exchange Current for Hydrogen Evolution, *J. Electrochem. Soc.*, 2005, **152**, J23.

40 L. Mallón, C. Cerezo-Navarrete, N. Romero, M. Puche, J. García-Antón, R. Bofill, K. Philippot, L. M. Martínez-Prieto and X. Sala, Ru nanoparticles supported on alginate-derived graphene as hybrid electrodes for the hydrogen evolution reaction, *New J. Chem.*, 2022, **46**, 49–56.

41 J. Creus, L. Mallón, N. Romero, R. Bofill, A. Moya, J. L. G. Fierro, R. Mas-Ballesté, X. Sala, K. Philippot and J. García-Antón, Ruthenium Nanoparticles Supported on Carbon Microfibers for Hydrogen Evolution Electrocatalysis, *Eur. J. Inorg. Chem.*, 2019, **2019**, 2071–2077.

42 I. Álvarez-Prada, D. Peral, M. Song, J. Muñoz, N. Romero, L. Escriche, A. Acharjya, A. Thomas, R. Schomäcker, M. Schwarze, X. Sala, M. Tasbihi and J. García-Antón, Ruthenium nanoparticles supported on carbon-based nanoallotropes as co-catalyst to enhance the photocatalytic hydrogen evolution activity of carbon nitride, *Renewable Energy*, 2021, **168**, 668–675.

43 S. Drouet, J. Creus, V. Collière, C. Amiens, J. García-Antón, X. Sala and K. Philippot, A porous Ru nanomaterial as an efficient electrocatalyst for the hydrogen evolution reaction under acidic and neutral conditions, *Chem. Commun.*, 2017, **53**, 11713–11716.

44 J. Lee, S. A. Sher Shah, P. J. Yoo and B. Lim, Hydrous RuO_2 nanoparticles as highly active electrocatalysts for hydrogen evolution reaction, *Chem. Phys. Lett.*, 2017, **673**, 89–92.

45 H. S. Park, J. Yang, M. K. Cho, Y. Lee, S. Cho, S. D. Yim, B. S. Kim, J. H. Jang and H. K. Song, RuO_2 nanocluster as a 4-in-1 electrocatalyst for hydrogen and oxygen electrochemistry, *Nano Energy*, 2019, **55**, 49–58.

46 J. Greeley, T. F. Jaramillo, J. Bonde, I. Chorkendorff and J. K. Nørskov, Computational high-throughput screening of electrocatalytic materials for hydrogen evolution, *Nat. Mater.*, 2006, **5**, 909–913.

47 Z. W. She, J. Kibsgaard, C. F. Dickens, I. Chorkendorff, J. K. Nørskov and T. F. Jaramillo, *Science*, 2017, **355**, eaad4998.

48 A. Moya, J. Creus, N. Romero, J. Alemán, X. Solans-Monfort, K. Philippot, J. García-Antón, X. Sala and R. Mas-Ballesté, Organocatalytic vs. Ru-based electrochemical hydrogenation of nitrobenzene in competition with the hydrogen evolution reaction, *Dalton Trans.*, 2020, **49**, 6446–6456.

49 A. Comas-Vives, K. Furman, D. Gajan, M. C. Akatay, A. Lesage, F. H. Ribeiro and C. Copéret, Predictive morphology, stoichiometry and structure of surface species in supported Ru nanoparticles under H_2 and CO atmospheres from combined experimental and DFT studies, *Phys. Chem. Chem. Phys.*, 2016, **18**, 1969–1979.

This journal is © the Partner Organisations 2023